ACS APPLIED ENERGY MATERIALS

www.acsaem.org Article

Molecular Engineering of Polyaniline with Ultrathin Polydopamine and Monolayer Graphene for All-Solid-State Flexible Microsupercapacitors

Muxuan Yang, Yanghe Liu, Xiongyu Luo, Yan Cao, Xiong Gong,* and Weinan Xu*

Cite This: *ACS Appl. Energy Mater.* 2021, 4, 10069−10080 Read Online

ACCESS | Metrics & More | Article Recommendations | Supporting Information

ABSTRACT: The use of conductive polyaniline (PANI) in energy storage has been extensively explored during the past several decades. Despite the significant progress, there is still a need for effective and simple methods to tune the structure and electrochemical performance of PANI at the molecular level, which are beyond conventional methods of mixing PANI with other materials. Here, we report a new approach for molecular engineering of PANI with ultrathin polydopamine and continuous monolayer graphene using a reactive layer-by-layer (LbL) deposition approach. Microsupercapacitors (MSCs) were fabricated based on the combination of reactive LbL deposition and lithography patterning. We discovered that the introduction of an ultrathin polydopamine layer between PANI layers leads to significant changes to the molecular structure, intermolecular spacing, and morphology of PANI. Those changes result in substantial improvements in the capacitance, stability, and flexibility of the hybrid MSCs. Furthermore, the use of continuous monolayer graphene as an atomically thin substrate for in situ polymerization of aniline leads to ultrathin PANI film with reduced charge-transfer resistance and improved electrochemical properties and stability. This work provides valuable insight into the structure and property control of conducting polymers, as well as the fabrication of soft and flexible energy storage devices.

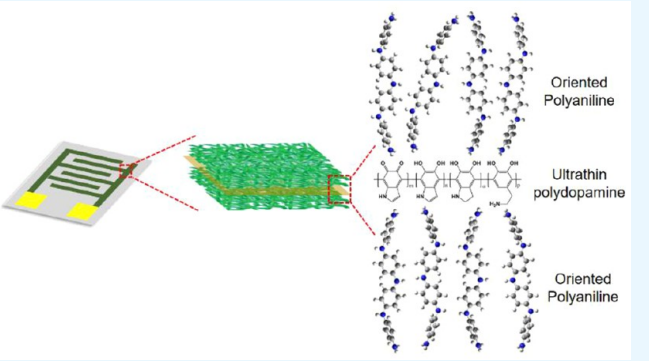

KEYWORDS: *polyaniline, polydopamine, graphene, reactive layer-by-layer deposition, microsupercapacitor*

INTRODUCTION

Miniaturized and flexible energy storage devices are in high demand in recent years due to the rapid development of soft and flexible electronics, sensors, and robotics.[1−4] Microsupercapacitors (MSCs), with their high power density, fast charge/discharge rate, and superior cyclic stability, have attracted much attention as the ideal microscale energy storage devices.[5−8] In-plane MSCs with interdigitated electrodes are especially attractive compared with conventional sandwich-type supercapacitors because of their small form factor, short pathway for ion transport, and the ease of integration with other types of electronic and sensing devices.[9−11]

The electrochemical active materials used for MSC fabrication are usually categorized into two classes based on their energy storage mechanisms: electrochemical double-layer materials and pseudocapacitive materials.[12] Pseudocapacitive materials store charge through redox reactions similar to a battery but at faster rates comparable to those of electrochemical double-layer capacitors. They have the potential to achieve both high energy and power densities.[13] Conducting polymers, such as polypyrrole, polythiophene, and polyaniline (PANI), which can exist in different oxidation states during redox reactions, have been widely used as pseudocapacitive materials.[14,15] Among them, PANI stands out because of its high conductivity and specific capacitance, flexibility, thermal stability, and low cost.[16,17] Importantly, PANI is easy to synthesize by chemical or electrochemical approaches and can form various nanostructures, including particles, fibers, rods, and flakes, depending on the chemistry and preparation conditions.[18−20]

On the other hand, PANI has its limitations in electrochemical stability and degradation at high potentials, which usually results in poor cycling stability and a limited working potential window for MSCs based on it.[21−23] The combination of PANI with other active materials such as carbon nanomaterials and metal oxides can overcome some of the intrinsic limitations.[24−26] Despite the tremendous progress achieved in this direction, there is still a strong need for the

Received: July 7, 2021
Accepted: August 23, 2021
Published: September 2, 2021

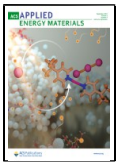

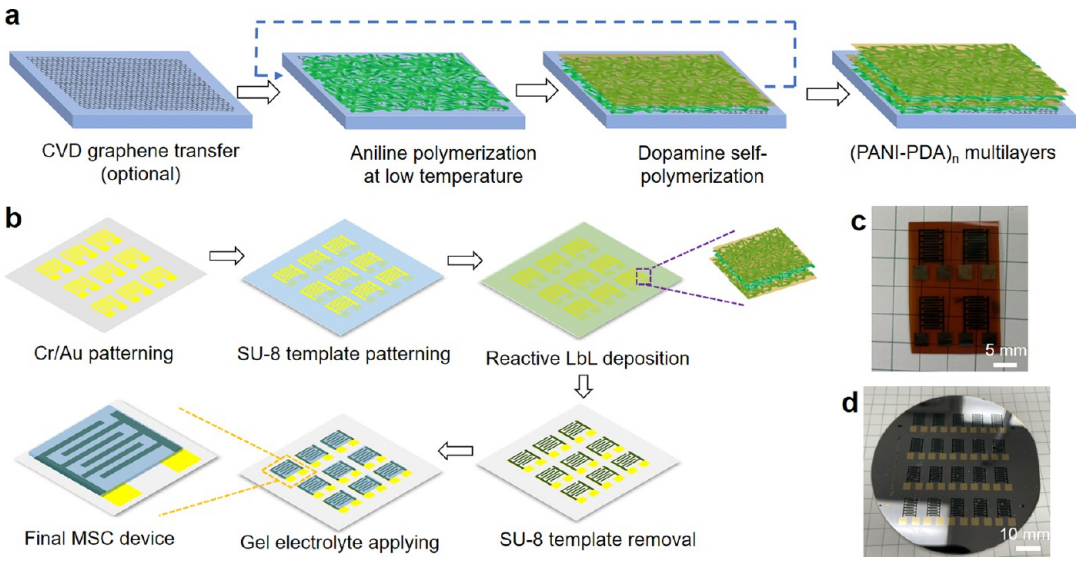

Figure 1. (a) Schematic of the reactive LbL deposition of $(PANI–PDA)_n$ hybrid thin films. (b) Fabrication process of interdigitated MSCs with $(PANI–PDA)_n$ as the electrode material. (c, d) Photos of the $(PANI–PDA)_n$ MSCs on a flexible polyimide substrate (c) and on a 3-in. Si wafer (d).

efficient modification or structural control of PANI with green and biobased materials in a low-cost way. Furthermore, the integration of PANI with biobased materials in a way that maintains or enhances its electrochemical properties, and at the same, compatible with lithography-based microfabrication is still a major challenge.[27]

Polydopamine (PDA) is a bioadhesive with excellent biocompatibility and multiple types of functional groups in its molecular structure.[28−30] It has been used for underwater adhesion and coatings on various surfaces, including those with very low surface energy, such as polytetrafluoroethylene.[31−34] Furthermore, it has also been demonstrated that PDA has certain levels of electrical conductivity depending on the conditions.[35−37] Therefore, the use of PDA in energy storage applications has been increasingly explored in recent years.[38,39] For instance, PDA was used as an additive to carbon cloth cathode in a Zn-ion hybrid supercapacitor,[40] it provides multiple redox-active sites like carbonyl groups for coordinating with alkali metal ions. PDA has also been used to increase the pseudocapacitance of carbon electrodes.[33,41] It can also work as a polymer glue to build up composites made of different types of carbon nanomaterials, including graphene[42] and carbon nanotube.[43] The integration of PDA with conducting polymers has also been explored to enhance the performance of bioelectronics.[44−46]

To the best of our knowledge, the integration of PDA with conducting polymers such as PANI in a precisely controlled way for MSC-based energy storage has never been studied before. Herein, we report a reactive layer-by-layer (LbL) polymerization approach for the integration of PANI and ultrathin PDA layers. The reactive LbL deposition is also combined with lithography patterning to fabricate flexible MSCs with patterned interdigital electrodes. We discovered that the ultrathin PDA layer significantly altered the morphology and molecular packing of PANI in the multilayered structure. As a result, the electrochemical performance, including specific capacitance, cycling stability, and mechanical stability, is greatly enhanced. In addition, we also studied the effect of continuous monolayer graphene as the substrate for in situ polymerization of polyaniline, which provides valuable insight into the PANI-based hybrid electroactive materials on a molecular level.

RESULTS AND DISCUSSION

Reactive LbL Deposition and MSC Fabrication. To achieve precise control over the morphology, thickness, and molecular orientation of the PANI-based electrode materials, we developed a reactive LbL deposition process of PANI with ultrathin PDA. As shown in Figure 1a, in the first step, PANI polymerization was conducted at low temperature in the presence of formic acid and NaCl, which enables the synthesis of PANI with relatively high molecular weight, crystallinity, as well as ordered molecular orientation.[47] In the second step, a thin layer of PDA was deposited on the surface of PANI by self-polymerization of dopamine. The PDA layer is important in promoting the adhesion and intimate contact between the PANI layers.[46] It also affects the molecular packing, crystallinity, and morphology of the PANI layer on top of it, as will be discussed later.

The PANI and PDA deposition processes can be repeated to get the multilayered structures, such as 1.5 bilayers and 2 bilayers electrode structures. As a control sample to study the effect of introducing ultrathin PDA layers between PANI, the sample with two consecutive layers of PANI deposition was also prepared. The samples with one layer of PANI, two consecutive PANI layers, PANI−PDA−PANI three layers, and PANI−PDA−PANI−PDA four layers are named as $PANI_1$, $PANI_2$, $(PANI–PDA)_{1.5}$, and $(PANI–PDA)_2$, respectively. Furthermore, to study the effect of continuous monolayer graphene as the substrate for in situ polymerization of aniline, we also prepared samples with a CVD graphene underneath the PANI, which are named as $G\text{-}PANI_1$.

The MSC fabrication is based on the combination of lithography patterning and the reactive LbL deposition of PANI and PDA, as shown in Figure 1b. The Au current collector was first deposited and patterned on the substrate, then the second step photolithography with SU-8 was conducted to generate a sacrificial deposition template. The

https://doi.org/10.1021/acsaem.1c01996
ACS Appl. Energy Mater. 2021, 4, 10069−10080

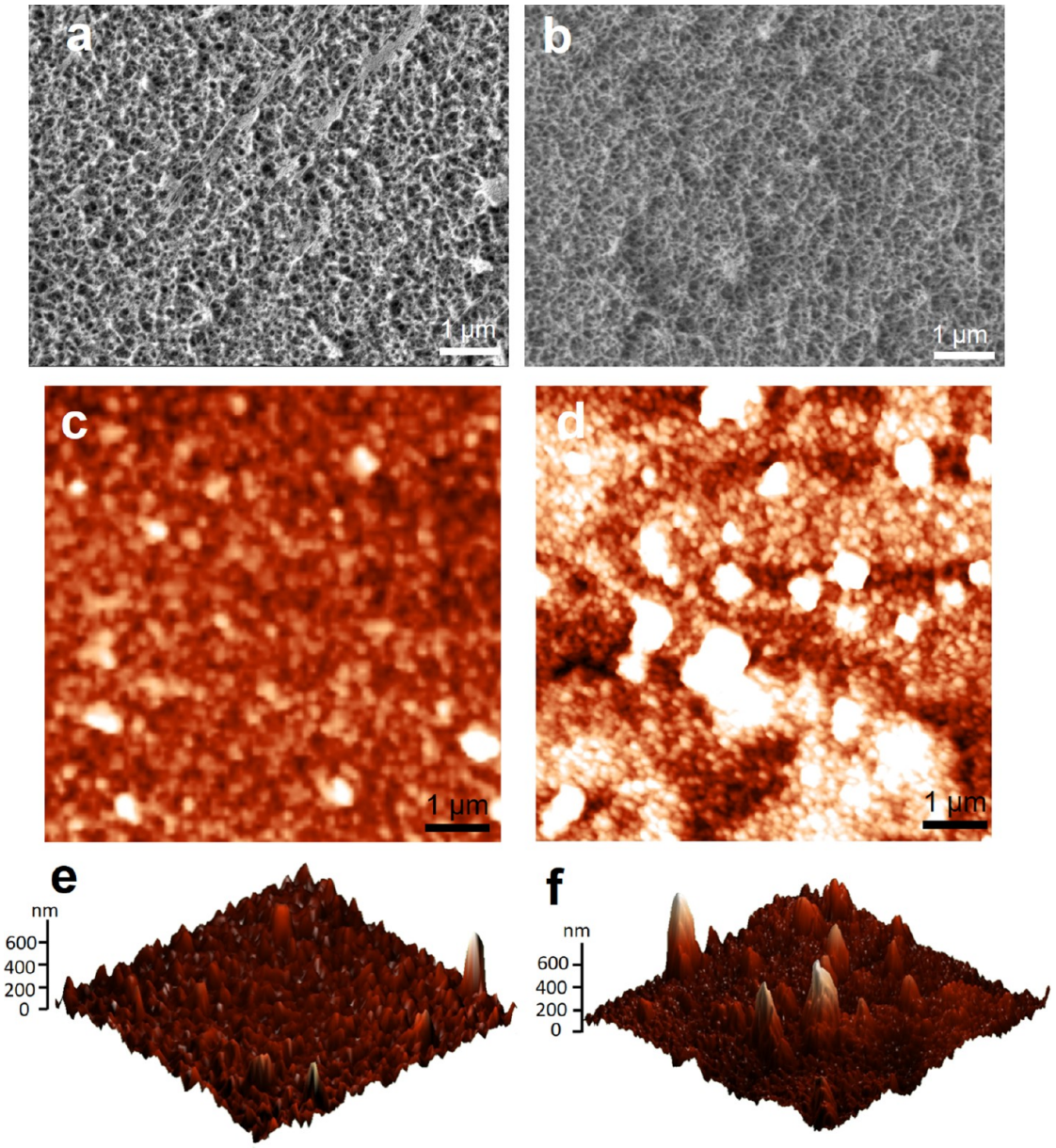

Figure 2. (a, b) SEM images of the $PANI_1$ (a) and G-$PANI_1$ (b) prepared by in situ polymerization of aniline at low temperature on the target substrate. (c, d) AFM topography images of the $PANI_1$ (c) and G-PAN_I (b). The *z* scale is 250 nm. (e, f) 3D representation of the 2D AFM images shown in panels c and d, respectively.

reactive LbL deposition of PANI and PDA was then conducted on the patterned substrate. After removing the SU-8 template, micropatterned electrodes are formed, and the PVA/H_2SO_4 gel electrolyte was applied on top of the electrodes.

One unique advantage of our reactive LbL deposition approach for microelectrode fabrication is that it can be done on a wide variety of substrates, including rigid and flexible ones. Figure 1c shows the MSCs fabricated on a flexible polyimide substrate. Figure 1d shows a large array of the MSCs fabricated on a rigid Si substrate. The overall size of the MSC and the electrode size can also be easily tuned by using different photomasks during the patterning process. For the MSC shown in this figure, each of the electrode fingers has a width of 400 μm, a length of 4 mm, and the interdigital distance is 200 μm.

Morphology of the PANI and (PANI−PDA)$_n$ Multilayers. The morphology of conducting polymers is directly related to their electrochemical and other properties. The morphology of the PANI-based hybrid electrodes was studied with SEM and AFM. $PANI_1$ shows a porous network structure with interconnected PANI nanofibers (average diameter = 50 nm). The pore sizes range from tens to hundreds of nm (Figure 2a). The nanoporous structure of the PANI thin film prepared by in situ polymerization of aniline at low temperature is important for its excellent ionic conductivity besides its intrinsic electrical conductivity. The thickness of $PANI_1$ is around 250 nm as measured by AFM cross-section analysis (Figure S1). Furthermore, the polymerization time has a significant effect on the thickness of the PANI film. The thickness gradually increases with the polymerization time. For 1 and 2 h of polymerization, the average PANI film thickness is 60 and 100 nm, respectively. The PANI film roughness also increases with polymerization time. We also found that the oxidative polymerization of aniline at a low temperature in our

https://doi.org/10.1021/acsaem.1c01996
ACS Appl. Energy Mater. 2021, 4, 10069−10080

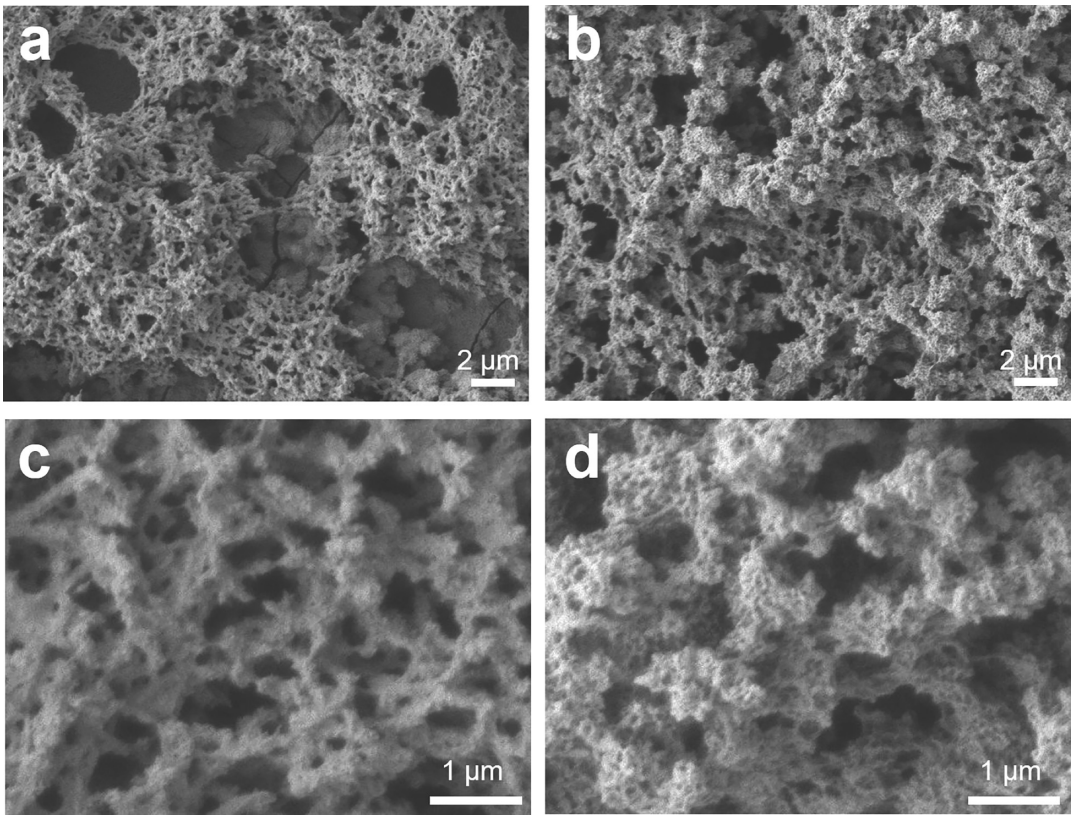

Figure 3. SEM images of the $PANI_2$ (a, c) and $(PANI–PDA)_{1.5}$ (b, d) at different magnifications. Both samples show nanoporous morphology but with different PANI nanostructures.

system reached equilibrium or saturation at around 3.5 h. Further increase of the polymerization time does not lead to a noticeable increase in the thickness or change in its morphology, as shown in Figure S2. But there is a shift in the absorption spectrum of PANI when polymerized for a longer time due to the higher doping extent by formic acid (Figure S3).

When a monolayer CVD graphene was used as the substrate for in situ polymerization of aniline, G-$PANI_1$ show a very similar network structure composed of PANI nanofibers (Figure 2b) and a similar thickness with $PANI_1$, which indicate the monolayer graphene does not significantly change the oxidation polymerization process of aniline. On the other hand, because of the template effect of the monolayer graphene, which is highly hydrophobic with intrinsic defects and wrinkles on the surface, the G-$PANI_1$ thin film has a higher surface roughness than the $PANI_1$ as measured by AFM (Figure 2c-f). The root-mean-square roughness of $PANI_1$ and G-$PANI_1$ over an area of 7 × 7 μm is 34 and 82 nm, respectively. The presence of monolayer graphene as an atomically thin conductive substrate as well as the resulting morphological change of PANI substantially affects the electrochemical performance, as will be discussed later.

To further increase the thickness and achieve precise control of the molecular structure of the PANI-based electrode materials, we developed the reactive LbL deposition with alternating PANI and PDA layers. The PDA layer is much thinner compared with the PANI layer due to its slow self-polymerization kinetics. The thickness of the PDA layer is about 15 nm under the polymerization condition used in our study (Figure S4). As a control sample to the $(PANI–PDA)_n$ multilayer materials, we also studied the $PANI_2$, which was prepared by two consecutive polymerization cycles (3.5 h for each) of aniline.

From the SEM images (Figure 3a, c), it can be seen that $PANI_2$ has a much more heterogeneous and porous morphology compared with $PANI_1$. The second layer PANI shows a rod-shaped morphology (average diameter: 200 nm) in contrast to the thin nanofiber structure in the first layer. Furthermore, the amount of PANI deposited from the second step polymerization is also much higher than that of the first step due to the preferential adsorption of the aniline monomers on the existing PANI layer (Figure S5). The average thickness of $PANI_2$ is 6.5 μm as measured from cross-section SEM images, which is significantly higher than that of $PANI_1$.

Importantly, the introduction of an ultrathin PDA as an intermediate layer between PANI significantly changed the morphology of the second PANI layer. Figure 3b and d show the morphology of $(PANI–PDA)_{1.5}$, which exhibits near-spherical 3D aggregates (several hundred nm in size) that interconnect with each other, and the 3D aggregates are composed of PANI nanofibers. $(PANI–PDA)_2$, which has an additional PDA layer on top, shows similar 3D morphology as $(PANI–PDA)_{1.5}$ (Figure S6). The thicknesses of the $(PANI–PDA)_{1.5}$ and $(PANI–PDA)_2$ are also around 6.5 μm due to the ultrathin nature of the PDA layer. Furthermore, the introduction of PDA makes the $(PANI–PDA)_n$ materials extremely hydrophilic, the $(PANI–PDA)_{1.5}$ has a contact angle of 0° (complete wetting), while the $PANI_2$ is more hydrophobic with a contact angle of 41.0° (Figure S7). The significant morphological and properties changes in PANI

https://doi.org/10.1021/acsaem.1c01996
ACS Appl. Energy Mater. 2021, 4, 10069−10080

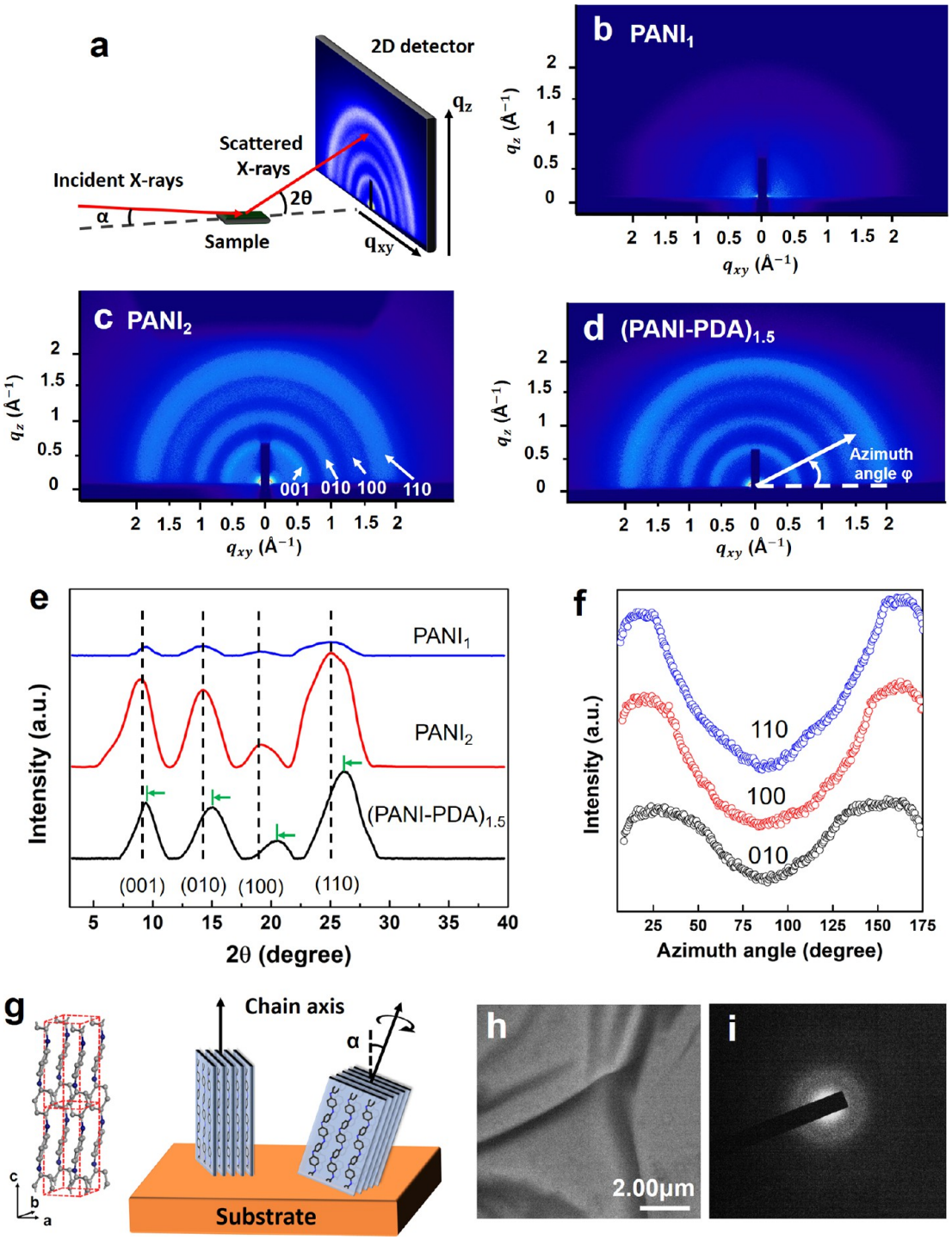

Figure 4. (a) Schematic illustration of the GIWAXS experiment. (b–d) 2D GIWXAS scattering patterns of $PANI_1$ (b), $PANI_2$ (c), and $(PANI–PDA)_{1.5}$ (d). (e) 1D GIWAXS profiles of $PANI_1$, $PANI_2$, and $(PANI–PDA)_{1.5}$. (f) Azimuthal scan profiles for the (110), (100), and (010) scattering of $(PANI–PDA)_{1.5}$. (g) Model of the pseudo-orthorhombic unit cell in PANI (left) and schematic of the end-on orientation of the PANI lamellae (right). (h) TEM bright-field image and (i) SAED pattern of the PANI thin film.

induced by the introduction of the PDA layer have major impacts on their performance as the electrode materials for MSCs, as will be discussed later.

Molecular Structure Characterization with GIWAXS. The transport properties of conducting polymers are strongly dependent on their molecular packing and ordering. In addition to the morphological study with SEM and AFM, we also used GIWAXS to study the structure of the PANI and $(PANI–PDA)_n$ at the molecular level (Figure 4a). The 2D scattering pattern for $PANI_1$ is shown in Figure 4b; the scattering intensity is weak because of its small thickness and relatively low crystallinity. The 2D GIWAXS patterns for $PANI_2$ and $(PANI–PDA)_{1.5}$ are shown in Figure 4c and d. They have much stronger scattering intensities compared with $PANI_1$, and there are four well-defined scattering rings, which

https://doi.org/10.1021/acsaem.1c01996
ACS Appl. Energy Mater. 2021, 4, 10069–10080

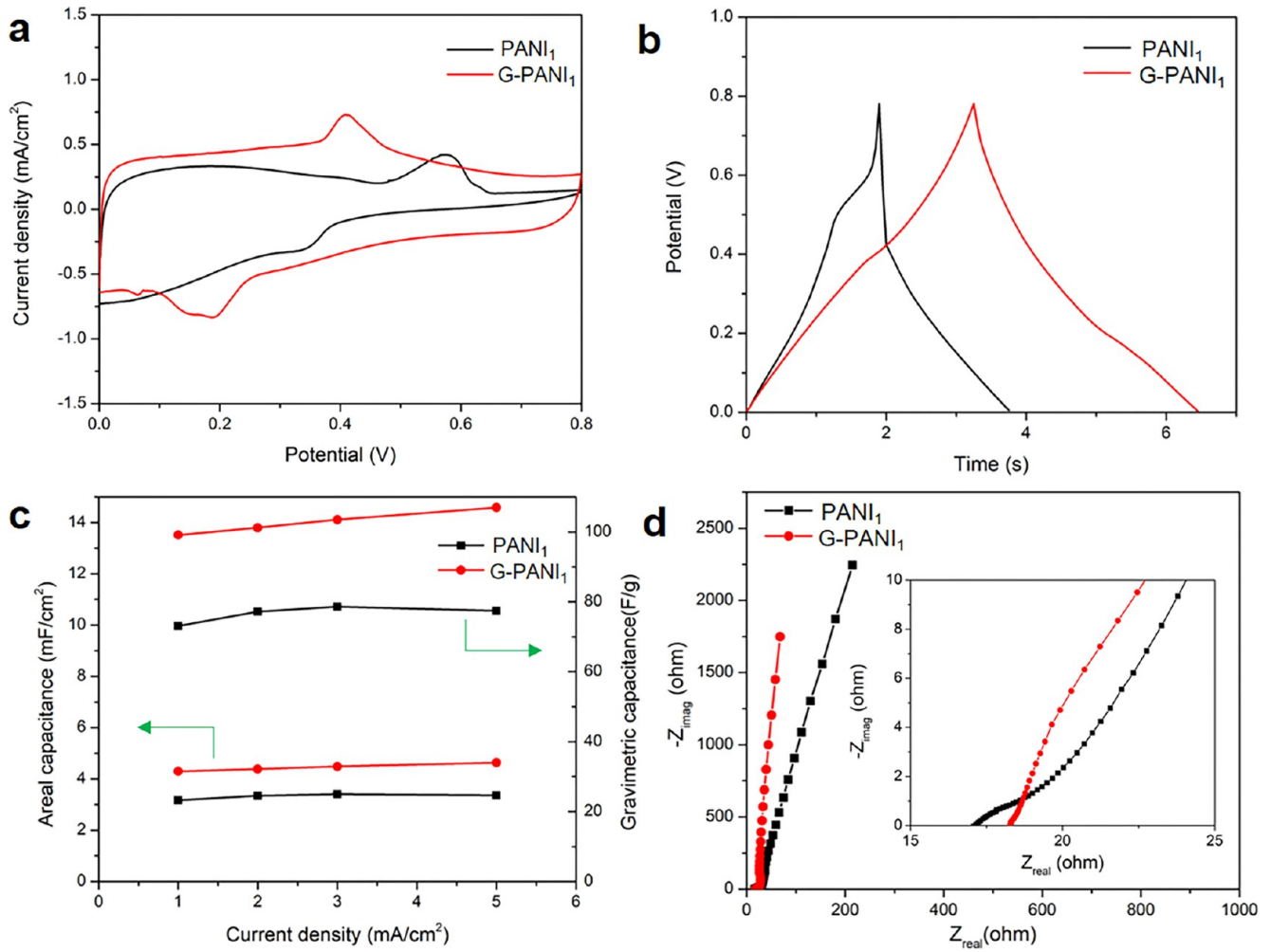

Figure 5. Electrochemical performance of the all-solid-state MSCs with $PANI_1$ and G-$PANI_1$ electrodes. (a) CV curves of the $PANI_1$ and G-$PANI_1$ MSCs obtained at a scan rate of 100 mV/s. (b) GCD curves for the $PANI_1$ and G-$PANI_1$ MSCs at a current density of 1 mA/cm^2. (c) Areal and gravimetric capacitances of the $PANI_1$ and G-$PANI_1$ MSCs at different current densities. (d) EIS plots of the $PANI_1$ and G-$PANI_1$ MSCs. The inset shows the magnified plot of the high-frequency range.

indicates the second layer of PANI has much higher crystallinity.

The 1D GIWAXS plots along the in-plane direction with respect to the scattering angle are shown in Figure 4e. For $PANI_1$, there are four relatively weak peaks at 0.64, 1.02, 1.42, and 1.77 Å^{-1}, which correspond to the (001), (010), (100), and (110) diffraction, respectively.[48,49] $PANI_2$ shows four diffraction peaks at the same q values but with much stronger intensity and well-defied shape. Interestingly, after introducing an ultrathin PDA layer between the two PANI layers, $(PANI–PDA)_{1.5}$ shows obvious shifts in the (001), (010), (100), and (110) peaks to higher q values (highlighted by green arrows in Figure 4e). For instance, the corresponding *d* spacings in the (001), (010), (100), and (110) directions decrease from 9.8, 6.1, 4.4, and 3.5 Å for $PANI_2$, to 9.3, 5.8, 4.2, and 3.4 Å, respectively, for $(PANI–PDA)_{1.5}$. This result shows that the presence of an ultrathin PDA has significant effects on the intermolecular spacing during the in situ polymerization of aniline. The second layer PANI has a more compact chain organization with smaller intermolecular spacing in all three directions.[50] Such molecular structure changes of PANI with the introduction of ultrathin PDA lead to substantial improvement in the electrochemical performance, as will be discussed later.

Furthermore, the azimuthal scans of the (010), (100), and (110) scattering show much stronger intensity close to the equator (when the azimuth angle is close to 0° and 180°), as shown in Figure 4f for $(PANI–PDA)_{1.5}$. The azimuthal scans for $PANI_1$ and $PANI_2$ also show stronger intensity close to the equator, but the difference is less pronounced (Figure S8). This is a strong indication that the PANI chains have a preferred orientation along the *c* axis or perpendicular to the substrate (Figure 4g), which is also called end-on orientation.[51] The $\pi–\pi$ stacking direction (*a*-axis direction) is parallel to the substrate. The TEM image of a single layer PANI thin film (Figure 4h) shows nanowrinkles on the sample. The SAED pattern from the PANI film (Figure 4i) shows the (100) diffraction ring (d = 4.4 Å), which is consistent with the GIWAXS results and indicates the end-on oriented PANI chains organize into lamellas along the *c* axis with various tilting angles.

We also studied and compared the electrical conductivity of the PANI and $(PANI–PDA)_n$ thin films (Figure S9). The $PANI_1$ has a conductivity of 1.85×10^{-3} S/cm, which is consistent with acid-doped PANI. $PANI_2$ has an increased

https://doi.org/10.1021/acsaem.1c01996
ACS Appl. Energy Mater. 2021, 4, 10069−10080

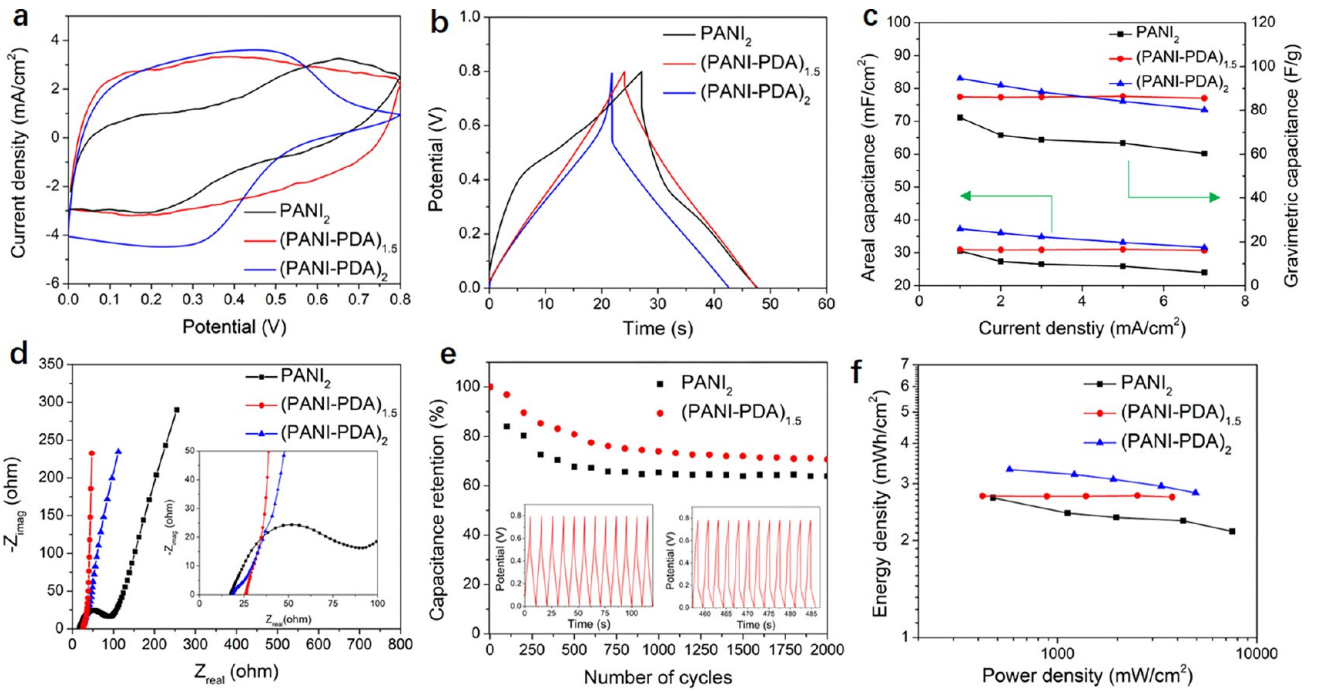

Figure 6. Electrochemical performance of the all-solid-state MSCs with $PANI_2$, $(PANI-PDA)_{1.5}$, and $(PANI-PDA)_2$ electrodes. (a) CV curves of the three types of MSCs obtained at a scan rate of 100 mV/s. (b) GCD curves of the three types of MSCs obtained at a current density of 1 mA/cm^2. (c) The areal and gravimetric capacitances of the three types of MSCs as a functional of current density. (d) EIS curves of the three types of MSCs, the inset shows the curves at the high-frequency range. (e) Cycling stability of $PANI_2$ and $(PANI-PDA)_{1.5}$ MSCs tested at a current density of 3 mA/cm^2, the insets are the GCD curves during the first and last 12 cycles. (f) Ragone plot of the three types of MSCs.

conductivity to 6.09×10^{-2} S/cm. After introducing the ultrathin PDA as the top layer, there is a pronounced drop in conductivity. For instance, $(PANI-PDA)_1$ has a conductivity of 4.29×10^{-4} S/cm, $(PANI-PDA)_2$ has a conductivity of 5.54×10^{-5} S/cm. When PANI is the top layer, the electrical conductivity is much higher: $(PANI-PDA)_{1.5}$ has a conductivity of 3.64×10^{-2} S/cm. The electrical conductivity plays an important role in their performance as the electrode materials for MSCs, as will be discussed in the following section.

Effect of Monolayer Graphene on the Performance of PANI MSCs. The capacitance of PANI-based supercapacitors usually has contributions from both electric double-layer capacitance and pseudocapacitance. PANI, in its conducting state (emeraldine salt), has good electrical conductivity so that electric double-layer capacitance can play a major role. On the other hand, PANI undergoes redox reactions with suitably applied potential, which leads to pseudocapacitance.

We first investigated the effect of monolayer CVD graphene on the electrochemical property and energy storage performance of in situ grown PANI thin films. To this purpose, we fabricated two types of interdigital MSCs with $PANI_1$ and G-$PANI_1$ as the electrode materials, respectively. The graphene was characterized by Raman (Figure S10), which shows sharp G and 2D bands with a high I_{2D}/I_G ratio. AFM characterization shows a smooth and uniform morphology with a thickness of 1.0 nm.

Representative CV curves measured at a scan rate of 100 mV/s, with a potential window of 0−0.8 V, are shown in Figure 5a. The $PANI_1$ MSC shows characteristic redox peaks for $PANI_1$, which is consistent with the pseudocapacitance behavior of PANI. On the other hand, the G-$PANI_1$ MSC shows a more rectangular-shaped CV curve with shifted redox peaks, the area within the curve is also significantly larger than that of $PANI_1$. This result indicates there is an additional contribution of electrical double-layer capacitance from the monolayer graphene besides the pseudocapacitance of PANI. The shape of the CV curve was better maintained at a high scan rate for G-$PANI_1$ than $PANI_1$ (Figure S11), demonstrating improved stability of the thin PANI film when grown from a monolayer graphene substrate.

The galvanostatic charge/discharge (GCD) curves at a current density of 1 mA/cm^2 are shown in Figure 5b. The $PANI_1$ MSC has a distorted charging curve, and there is a large instantaneous voltage drop (IR drop) at the beginning of the discharging curve. On the other hand, The G-$PANI_1$ GCD curve exhibit a trigonometric shape at different current densities (see also Figure S11), and there is almost no IR drop. This result indicates G-$PANI_1$ MSC has lower internal resistance and better stability.

The areal and gravimetric capacitances of the $PANI_1$ and G-$PANI_1$ MSCs were calculated based on the GCD curves (Figure 5c). It can be seen that both MSCs show very stable capacitance over the measured range of current density. The $PANI_1$ MSC has an areal capacitance of 3.4 mF/cm^2 and gravimetric capacitance of 77.5 F/g at 5 mA/cm^2. The G-$PANI_1$ MSC has an obviously higher areal capacitance of 4.6 mF/cm^2 and gravimetric capacitance of 107.0 F/g at the same current density.

The electrochemical impedance spectroscopy (EIS) data of $PANI_1$ and G-$PANI_1$ MSCs are shown in Figure 5d. The equivalent series resistance (ESR) obtained from the x-intercept of the Nyquist plot, which represents a summation of various contributions, including the active material ohmic resistance, the interface resistance of the active material/current collector, the electrolyte ionic resistance, is 17.1 ohm

https://doi.org/10.1021/acsaem.1c01996
ACS Appl. Energy Mater. 2021, 4, 10069−10080

for $PANI_1$ MSC, and 18.3 ohm for G-$PANI_1$ MSC. The Nyquist plot of $PANI_1$ MSC shows a semicircle at the high-frequency range and a straight line at the low-frequency range. The G-$PANI_1$ MSC, on the other hand, shows almost no semicircle in the Nyquist plot at the high-frequency range. The slope of the straight line at the low-frequency range is also obviously higher than that of $PANI_1$ MSC. Those results indicate that G-$PANI_1$ MSC has better electrical conductivity and lower charge-transfer resistance.[52] The intimate contact between continuous and large-area monolayer graphene and thin PANI film improves the charge transfer efficiency and reduces current leakage.

Electrochemical Performance of the $(PANI-PDA)_n$ MSCs. To improve the energy storage capability of the in situ polymerized PANI-based MSCs, the thickness of the PANI-based electrodes, as well as their molecular structures and chain packing needs to be precisely controlled. We achieved this by using the reactive LbL deposition of PANI and PDA combined with a lithography patterned template as described above. Besides its unique properties as a bioadhesive, PDA is also considered as a disordered organic semiconductor.[53] Its introduction to the multilayered PANI has the potential to improve stability and electrochemical performance.

We compared the performance of three types of MSCs, namely, $(PANI-PDA)_{1.5}$, $(PANI-PDA)_2$, and a control sample $PANI_2$ which has two consecutive layers of PANI but without PDA in between. CV curves for the three types of MSCs at a scan rate of 100 mV/s (Figure 6a) show obvious differences (see also Figure S12). The CV curve for $PANI_2$ MSC deviates from the rectangle shape and has two pairs of broad redox peaks, which is attributed to the leucoemeraldine/emeraldine/pernigraniline transitions of PANI, confirming the pseudocapacitance behavior of the conducting polymer.[38]

Interestingly, after introducing an ultrathin PDA between the two PANI layer, the $(PANI-PDA)_{1.5}$ MSC exhibit a quasi-rectangular shaped CV curve, with much a larger area within the curve. The $(PANI-PDA)_2$MSC has a similar rectangle-shaped CV curve except at the high potential range. The current drop at high potential is most likely due to the resistance increase when PDA is the top layer. The CV scans at different current densities of those three types of devices are shown in Figure S12.

The GCD curves for the three types of MSCs are shown in Figure 6b (see also Figure S12). $PANI_2$ MSC shows a distorted charge curve and a large IR drop in the discharge curve. On the other hand, the $(PANI-PDA)_{1.5}$ MSC exhibit almost perfectly triangular charge and discharge curves with very small IR drop. The $(PANI-PDA)_2$ MSC also shows a triangular-shaped curve but with a larger IR drop, which is again attributed to the increased resistance with the PDA layer is on top. The areal and gravimetric capacitance was calculated from the GCD curves and summarized in Figure 6c. $(PANI-PDA)_{1.5}$ and $(PANI-PDA)_2$ MSCs have much higher capacitances than the $PANI_2$ MSC. For instance, the areal capacitances of $PANI_2$, $(PANI-PDA)_{1.5}$, and $(PANI-PDA)_2$ MSCs at 5 mA/cm^2 are 25.9, 31.0, and 33.2 mF/cm^2; the gravimetric capacitances are 65.0, 86.4, and 84.1 F/g, respectively. Furthermore, the $(PANI-PDA)_{1.5}$ MSC shows outstanding stability in capacitance over the measured range of current density. In comparison, the $PANI_2$ MSC has a noticeable decrease in capacitance with increasing current density.

The EIS curves for $PANI_2$ MSC, $(PANI-PDA)_{1.5}$ and $(PANI-PDA)_2$MSCs also show significantly different characters (Figure 6d). $PANI_2$ MSC shows a large semicircle in the high-frequency range of the EIS curve, the $(PANI-PDA)_{1.5}$ MSC shows no semicircle at all, and the $(PANI-PDA)_2$ MSC shows a very small semicircle. Moreover, the slopes of the straight-line part of the EIS curves are quite different, with $PANI_2$ MSC has the smallest slope, and $(PANI-PDA)_{1.5}$ has the largest slope. This result is another strong evidence that the introduction of ultrathin PDA dramatically improves the ion transport in the electrode materials. Our lithography-based MSC fabrication approach allows flexible design of the interdigital device geometry. For instance, the electrode finger width, finger spacing, and the number of fingers can all be adjusted by using different photomasks. Generally, an increase in figure number or narrowing the finger width can efficiently decrease the ionic diffusion pathway and reduce electrolyte resistance with low ion transport limitations.[10,54]

The significant improvement in electrochemical performance of PANI after the introduction of the PDA layer can be related to the dramatic changes in morphology and molecular structures as demonstrated with SEM and GIWAXS. The second layer of PANI in $PANI_2$ shows a rod-shaped morphology with a large diameter. In contrast, the second layer of PANI in $(PANI-PDA)_{1.5}$ and $(PANI-PDA)_2$ shows near-spherical 3D assembled structures composed of PANI nanofibers. As a result, the $(PANI-PDA)_{1.5}$ and $(PANI-PDA)_2$ have much higher active surface area, which facilitates ion and charge transport,[55] as well as a larger contribution from electrochemical double-layer capacitance. The GIWAXS results show that the PANI chains in $(PANI-PDA)_{1.5}$ have a more compact molecular organization than $PANI_2$, which is another factor promoting the ion and charge transport. In addition, the enhanced hydrophilicity of $(PANI-PDA)_{1.5}$ enables intimate contact between the gel electrolytes and the electrodes.

MSCs based on conducting polymers, including PANI, usually have poor long-term cycling stability because of the swelling and shrinking of the polymers during the doping/dedoping process. The long-term cycle stability data for $PANI_2$ MSC are shown in Figure 6e; the capacitance has a substantial drop after the first 1000 cycles to 65% of its initial value and, then, remains stable at around 64% with further cycles. On the other hand, the $(PANI-PDA)_{1.5}$ MSCs show obviously improved cycling stability. The capacitance drop after 1000 cycles is improved to 74% of the initial value, and it is stably maintained at 71% with 2000 and further cycles. This result is significant considering that there is no additional carbon or other inorganic materials added to the PANI; only an ultrathin (~15 nm) PDA layer was introduced between the PANI layers. The cycling stability of the $(PANI-PDA)_n$ MSCs can be further improved when combing with inorganic nanomaterials to make hybrid electrodes.[56]

The Ragone plot showing both the energy and power density of the three types of MSCs is in Figure 6f. It can be seen that $PANI_2$ MSC has an obvious decrease in energy density at high power density. The $(PANI-PDA)_{1.5}$ MSC has superior stability with a minimum drop in energy density. The $(PANI-PDA)_2$ MSC has a noticeable decrease in energy density at high power density due to the increased resistance induced by the top PDA layer.

Another advantage of our reactive LbL approach for the fabrication of micropatterned PANI−PDA electrodes is that it

https://doi.org/10.1021/acsaem.1c01996
ACS Appl. Energy Mater. 2021, 4, 10069−10080

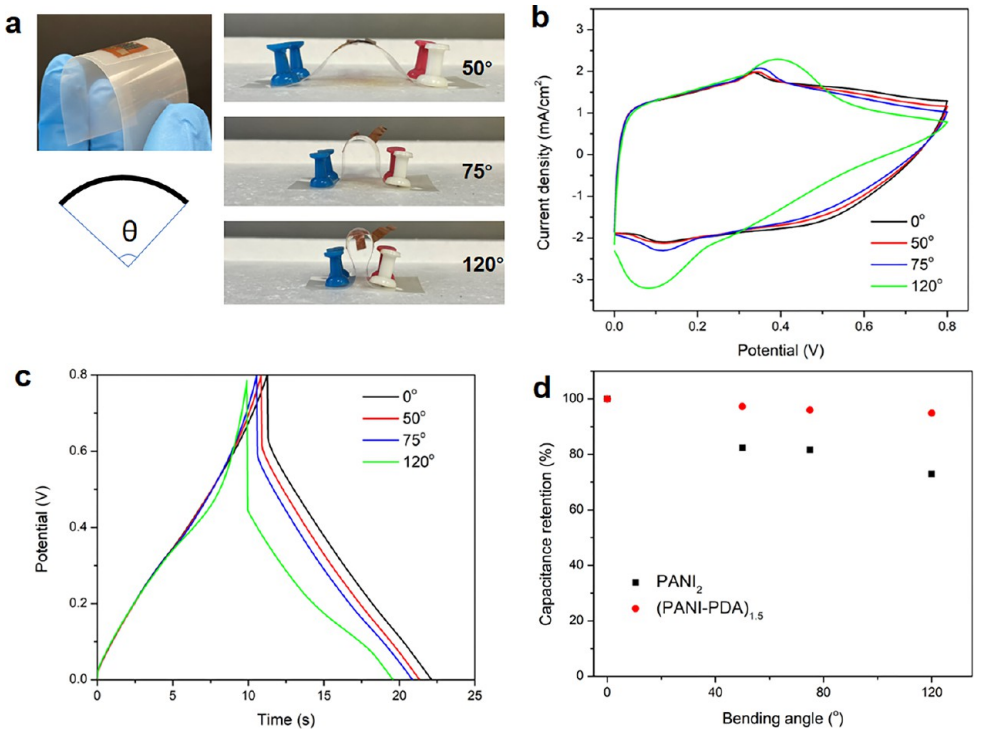

Figure 7. Mechanical flexibility of the $(PANI–PDA)_n$ MSCs. (a) Photos of the devices in the different bending states. (b) CV curves for the $(PANI–PDA)_{1.5}$ MSC at different bending angles, and the scan rate is 50 mV/s. (c) GCV curves for the $(PANI–PDA)_{1.5}$ MSC at different bending angles, and the current density is 2 mA/cm^2. (d) Capacitance changes of $PANI_2$ and $(PANI–PDA)_{1.5}$ MSCs as a function of bending angles.

can be applied to a wide variety of substrates, including rigid and flexible ones. We studied and compared the performance of the flexible $PANI_2$ and $(PANI–PDA)_{1.5}$ MSCs when they are subjected to bending deformations. The flexible MSC device was placed on a flexible polyester carrier substrate, and the bending angle is measured and calculated from the bending extent of the substrate (Figure 7a).

The $(PANI–PDA)_{1.5}$ MSC shows excellent stability against bending even at large angles. For instance, the capacitance retention is at 95% at a large bending angle of 120°. The CV and GCD curves are very close to that of the flat state when the bending angle is smaller than 120° (Figure 7b and c). The GCD curve at 120° bending shows a higher IR drop in the discharge part, which indicates an increase in the internal resistance at very high bending angles, but the overall capacitance is still well maintained (Figure 7d).

In comparison, the $PANI_2$ MSC has a substantial drop in capacitance when subjected to bending deformation. The CV curves show larger decreases in the area, and the GCD curves have larger decreases in charge/discharge time with increasing bending angle (Figure S13). As a result, the capacitance of $PANI_2$ MSC drops to 82% and 73% of its initial value when the bending angles are 50° and 120°, respectively. The better electrochemical performance of the $(PANI–PDA)_n$ MSCs during mechanical deformation is attributed to the introduction of an ultrathin PDA layer, which acts as an efficient bioadhesive between PANI layers. In addition, the morphological and molecular structure changes in PANI induced by the ultrathin PDA are also important reasons.

Furthermore, the output potential and current window of the $(PANI–PDA)_n$ MSC can be increased by connecting multiple devices in series or parallel configuration. We showed that by connecting multiple (two, three, and four) $(PANI–PDA)_2$ MSCs in series, it provided a corresponding multiple times higher operation potential window (Figure S14). When two MSCs were connected in parallel, the current density and the discharge time increased to 2-fold of those in a single MSC device. Our lithography-based microfabrication enables facile design and production of the connected MSC arrays on a large scale for practical applications.

CONCLUSION

In conclusion, a new approach to control the molecular structure and enhance the electrochemical performance of PANI was developed. This approach is based on the reactive LbL deposition of alternating layers of PANI and ultrathin PDA by in situ polymerization of their monomers. All-solid-state MSCs were fabricated by combining the reactive LbL deposition of $(PANI–PDA)_n$ electrodes with lithography patterning. The presence of an ultrathin PDA layer significantly affects the molecular structure, intermolecular spacing, and morphology of the PANI, as confirmed by SEM, AFM, and GIWAXS characterization. The morphological and structural changes lead to substantial improvement in the performance of the MSCs based on $(PANI–PDA)_n$ electrodes. We also discovered that using continuous monolayer graphene as the polymerization template for PANI results in enhanced charge transfer efficiency and electrochemical stability. Our findings are valuable for the rational design and structural control of conducting polymer using biomaterials, as well as the fabrication of miniaturized and flexible energy storage devices with hierarchical structures.

EXPERIMENTAL SECTION

Materials. Dopamine hydrochloride, ammonium persulfate, poly(vinyl alcohol) hydrolyzed (M_w = 85 000–124 000 Da) were purchased from Sigma-Aldrich. Sodium chloride was purchased from EMD chemicals. Tris-HCl was purchased from Thermo

https://doi.org/10.1021/acsaem.1c01996
ACS Appl. Energy Mater. 2021, 4, 10069–10080

Scientific. Aniline was purchased from Millipore Sigma. Formic acid and sulfuric acid were purchased from Fisher Scientific. Acetone and isopropanol were purchased from VWR. S1805 photoresist, MF319 developer, SU-8 2075 photoresist, and SU-8 developer were purchased from Kayaku Advanced Materials, Inc. CVD graphene was purchased from ACS Material, LLC.

In Situ Polymerization of Aniline at Low Temperature. Polyaniline with high molecular weight and crystallinity was synthesized directly on the substrate by oxidative polymerization of aniline at low temperature in the presence of acid and salt. The target substrate was placed inside the reaction container before the polymerization starts. Aniline monomer (0.2 mL) was dissolved in formic acid (5 M aqueous solution) and sodium chloride (4.2 M). Ammonium persulfate was used as the oxidant. The high concentration of NaCl salt was to ensure that the reaction medium was in the liquid state at a low temperature. The monomer and oxidant solutions were precooled to 0 °C. After mixing, the reactor was kept at −20 °C for 3.5 h. Then, the substrate was removed from the reaction, rinsed with formic acid (5 M) aqueous solution and DI water, and dried under ambient condition.

Self-Polymerization of Dopamine. The self-polymerization of dopamine was conducted to form an ultrathin polydopamine layer directly on the target materials. Dopamine hydrochloride (3 mg/mL) was dissolved in 0.01 M Tris-HCl buffer solution with a pH of 8.5, and the target substrate was immersed in the solution. The reaction was conducted for 16 h at room temperature. The substrate was then removed from the solution, rinsed thoroughly with DI water, and dried under ambient condition.

Fabrication of Microsupercapacitors. The fabrication process of the MSCs is shown in Figure 1b. The MSCs can be fabricated on both rigid substrates (Si wafer) and flexible substrates (polyimide film). The micropatterned Cr/Au (5/50 nm) current collector was deposited on the substrate by photolithography, followed by thermal evaporation and metal lift-off. The substrate with micropatterned current collector was then used for the second step of photolithography to generate SU-8 patterns that cover the whole substrate except the current collector area. The substrate was then used to deposit PANI and PDA by the reactive LbL deposition process as described above. After the desired number of layers of PANI and PDA were deposited, the sacrificial SU-8 pattern was removed from the substrate by delaminating in acetone. Then the device was rinsed with acetone and isopropanol, then dried with compressed air. Finally, the PVA/H_2SO_4 gel electrolyte was applied to the top of the micropatterned electrodes. The fabrication of G-PANI MSC follows the same procedure, except that there was an additional CVD graphene transfer and patterning step before the deposition of PANI layer.

Characterization. Atomic force microscopy (AFM) characterization was done with the NT-MDT SMENA system, the images were acquired in tapping mode with 300 kHz resonance frequency Si cantilevers, and the scan rate was set at 0.5 Hz. Scanning electron microscopy (SEM) was conducted using JEOL-7401 FE-SEM at an accelerating voltage of 10 kV. UV−vis spectra were collected with the Agilent Cary-60 Spectrometer. Electrical conductivity measurements were conducted with a Keithley 2400 source meter. Sample weight measurements were conducted with a Sartorius microbalance.

Grazing incidence wide-angle X-ray scattering (GIWAXS) experiments were carried by using Rigaku RAOID II, equipped with Hypix-600 detector and FR-X rotating-anode X-ray source (λ = 0.154 nm) under the working voltage of 45 kV and current of 66 mA. The incident X-ray hit on the sample with the scattering angle 2θ varied from 0.8° to 40°. The samples for GIWAXS were prepared by the same reactive LbL deposition method on a silicon wafer as described above.

Transmission electron microscopy (TEM) bright-field images and selected-area electron diffraction (SAED) patterns were obtained by a JEOL-1400 TEM at an acceleration voltage of 110 kV. The *d*-spacing of the SAED patterns in PANI was calibrated with an aluminum standard.

Electrochemical Measurement. The measurements were conducted with a CHI 660D electrochemical workstation and a Gamry reference 3000 electrochemical workstation. Cyclic voltammetry (CV) was measured at different scan rates ranging from 1 to 100 mV/s. Galvanostatic charge and discharge (GCD) was measured at different current densities from 1 to 10 mA/cm^2. Electrochemical impedance spectroscopy (EIS) was recorded between a frequency range of 0.1 Hz−1 MHz. The capacitance calculation from the measured data was described in the SI.

■ ASSOCIATED CONTENT

Supporting Information

The Supporting Information is available free of charge at https://pubs.acs.org/doi/10.1021/acsaem.1c01996.

SEM images, UV−vis spectra, Raman spectra, AFM, contact angle, GIWAXS, and conductivity data (PDF)

■ AUTHOR INFORMATION

Corresponding Authors

Xiong Gong − *School of Polymer Science and Polymer Engineering, The University of Akron, Akron, Ohio 44325, United States;* orcid.org/0000-0001-6525-3824; Email: xgong@uakron.edu

Weinan Xu − *School of Polymer Science and Polymer Engineering, The University of Akron, Akron, Ohio 44325, United States;* orcid.org/0000-0002-5352-3302; Email: weinanxu@uakron.edu

Authors

Muxuan Yang − *School of Polymer Science and Polymer Engineering, The University of Akron, Akron, Ohio 44325, United States*

Yanghe Liu − *School of Polymer Science and Polymer Engineering, The University of Akron, Akron, Ohio 44325, United States*

Xiongyu Luo − *School of Polymer Science and Polymer Engineering, The University of Akron, Akron, Ohio 44325, United States*

Yan Cao − *Institute for Advanced Study, Shenzhen University, Guangdong 518060, China;* orcid.org/0000-0001-8897-8385

Complete contact information is available at: https://pubs.acs.org/10.1021/acsaem.1c01996

Notes

The authors declare no competing financial interest.

■ ACKNOWLEDGMENTS

W.X. gratefully acknowledge the startup support from the University of Akron. Y.L. and X.G. thank the National Science Foundation (ECCS/EPMD1903303) for financial supports. The authors would like to thank Pratik Kasbe for AFM and Raman measurements.

■ REFERENCES

(1) Zheng, S.; Shi, X.; Das, P.; Wu, Z. S.; Bao, X. The Road Towards Planar Microbatteries and Micro-Supercapacitors: From 2D to 3D Device Geometries. *Adv. Mater.* **2019**, *31*, 1900583.

(2) Kyerematen, N. A.; Brousse, T.; Pech, D. Microsupercapacitors as Miniaturized Energy-Storage Components for on-Chip Electronics. *Nat. Nanotechnol.* **2017**, *12*, 7−15.

(3) Pan, S.; Ren, J.; Fang, X.; Peng, H. Integration: An Effective Strategy to Develop Multifunctional Energy Storage Devices. *Adv. Energy Mater.* **2016**, *6*, 1501867.

(4) Sumboja, A.; Liu, J.; Zheng, W. G.; Zong, Y.; Zhang, H.; Liu, Z. Electrochemical Energy Storage Devices for Wearable Technology: A Rationale for Materials Selection and Cell Design. *Chem. Soc. Rev.* **2018**, *47*, 5919−5945.
(5) Hu, H.; Pei, Z.; Ye, C. Recent Advances in Designing and Fabrication of Planar Micro-Supercapacitors for on-Chip Energy Storage. *Energy Storage Mater.* **2015**, *1*, 82−102.
(6) Lv, T.; Liu, M.; Zhu, D.; Gan, L.; Chen, T. Nanocarbon-Based Materials for Flexible All-Solid-State Supercapacitors. *Adv. Mater.* **2018**, *30*, 1705489.
(7) Kim, D.; Shin, G.; Kang, Y. J.; Kim, W.; Ha, J. S. Fabrication of a Stretchable Solid-State Micro-Supercapacitor Array. *ACS Nano* **2013**, *7*, 7975−7982.
(8) Wang, J.; Li, F.; Zhu, F.; Schmidt, O. G. Recent Progress in Micro-Supercapacitor Design, Integration, and Functionalization. *Small Methods* **2019**, *3*, 1800367.
(9) Zhang, J.; Zhang, G.; Zhou, T.; Sun, S. Recent Developments of Planar Micro-Supercapacitors: Fabrication, Properties, and Applications. *Adv. Funct. Mater.* **2020**, *30*, 1910000.
(10) Wu, Z. S.; Parvez, K.; Feng, X.; Müllen, K. Photolithographic Fabrication of High-Performance All-Solid-State Graphene-Based Planar Micro-Supercapacitors with Different Interdigital Fingers. *J. Mater. Chem. A* **2014**, *2*, 8288−8293.
(11) Liu, N.; Gao, Y. Recent Progress in Micro-Supercapacitors with In-Plane Interdigital Electrode Architecture. *Small* **2017**, *13*, 1701989.
(12) Zhong, C.; Deng, Y.; Hu, W.; Qiao, J.; Zhang, L.; Zhang, J. A Review of Electrolyte Materials and Compositions for Electrochemical Supercapacitors. *Chem. Soc. Rev.* **2015**, *44*, 7484−7539.
(13) Choi, C.; Ashby, D. S.; Butts, D. M.; DeBlock, R. H.; Wei, Q.; Lau, J.; Dunn, B. Achieving High Energy Density and High Power Density with Pseudocapacitive Materials. *Nat. Rev. Mater.* **2020**, *5*, 5−19.
(14) Lin, Z.; Goikolea, E.; Balducci, A.; Naoi, K.; Taberna, P. L.; Salanne, M.; Yushin, G.; Simon, P. Materials for Supercapacitors: When Li-Ion Battery Power Is Not Enough. *Mater. Today* **2018**, *21*, 419−436.
(15) Shi, Y.; Peng, L.; Ding, Y.; Zhao, Y.; Yu, G. Nanostructured Conductive Polymers for Advanced Energy Storage. *Chem. Soc. Rev.* **2015**, *44*, 6684−6696.
(16) Li, H.; Wang, J.; Chu, Q.; Wang, Z.; Zhang, F.; Wang, S. Theoretical and Experimental Specific Capacitance of Polyaniline in Sulfuric Acid. *J. Power Sources* **2009**, *190*, 578−586.
(17) Liu, P.; Yan, J.; Guang, Z.; Huang, Y.; Li, X.; Huang, W. Recent Advancements of Polyaniline-Based Nanocomposites for Supercapacitors. *J. Power Sources* **2019**, *424*, 108−130.
(18) Baker, C. O.; Huang, X.; Nelson, W.; Kaner, R. B. Polyaniline Nanofibers: Broadening Applications for Conducting Polymers. *Chem. Soc. Rev.* **2017**, *46*, 1510−1525.
(19) Wang, X.; Xu, M.; Fu, Y.; Wang, S.; Yang, T.; Jiao, K. A Highly Conductive and Hierarchical PANI Micro/Nanostructure and Its Supercapacitor Application. *Electrochim. Acta* **2016**, *222*, 701−708.
(20) Eftekhari, A.; Li, L.; Yang, Y. Polyaniline Supercapacitors. *J. Power Sources* **2017**, *347*, 86−107.
(21) Cong, H. P.; Ren, X. C.; Wang, P.; Yu, S. H. Flexible Graphene-Polyaniline Composite Paper for High-Performance Supercapacitor. *Energy Environ. Sci.* **2013**, *6*, 1185−1191.
(22) Song, B.; Tuan, C. C.; Huang, X.; Li, L.; Moon, K. S.; Wong, C. P. Sulfonated Polyaniline Decorated Graphene Nanocomposites as Supercapacitor Electrodes. *Mater. Lett.* **2016**, *166*, 12−15.
(23) Song, B.; Li, L.; Lin, Z.; Wu, Z.-K.; Moon, K.-s.; Wong, C.-P. Water-Dispersible Graphene/Polyaniline Composites for Flexible Micro-Supercapacitors with High Energy Densities. *Nano Energy* **2015**, *16*, 470−478.
(24) Wu, Z. S.; Parvez, K.; Li, S.; Yang, S.; Liu, Z.; Liu, S.; Feng, X.; Müllen, K. Alternating Stacked Graphene-Conducting Polymer Compact Films with Ultrahigh Areal and Volumetric Capacitances for High-Energy Micro-Supercapacitors. *Adv. Mater.* **2015**, *27*, 4054−4061.
(25) Zhang, K.; Zhang, L. L.; Zhao, X. S.; Wu, J. Graphene/Polyaniline Nanofiber Composites as Supercapacitor Electrodes. *Chem. Mater.* **2010**, *22*, 1392−1401.
(26) Wu, Q.; Xu, Y.; Yao, Z.; Liu, A.; Shi, G. Supercapacitors Based on Flexible Graphene/Polyaniline Nanofiber Composite Films. *ACS Nano* **2010**, *4*, 1963−1970.
(27) Wang, K.; Zou, W.; Quan, B.; Yu, A.; Wu, H.; Jiang, P.; Wei, Z. An All-Solid-State Flexible Micro-Supercapacitor on a Chip. *Adv. Energy Mater.* **2011**, *1* (6), 1068−1072.
(28) Ryu, J. H.; Messersmith, P. B.; Lee, H. Polydopamine Surface Chemistry: A Decade of Discovery. *ACS Appl. Mater. Interfaces* **2018**, *10*, 7523−7540.
(29) Krishnamoorthy, M.; Hakobyan, S.; Ramstedt, M.; Gautrot, J. E. Surface-Initiated Polymer Brushes in the Biomedical Field: Applications in Membrane Science, Biosensing, Cell Culture, Regenerative Medicine and Antibacterial Coatings. *Chem. Rev.* **2014**, *114*, 10976−11026.
(30) Liu, S.; Kasbe, P. S.; Yang, M.; Shen, N.; Duan, L.; Mao, Y.; Xu, W. Intimately Bonded 2D Materials and Responsive Polymer Brushes for Adaptive Nanocomposites. *Polymer* **2020**, *210*, 123033.
(31) Qu, K.; Wang, Y.; Vasileff, A.; Jiao, Y.; Chen, H.; Zheng, Y. Polydopamine-Inspired Nanomaterials for Energy Conversion and Storage. *J. Mater. Chem. A* **2018**, *6*, 21827−21846.
(32) Zhang, Y.; Yin, X.; Yu, B.; Wang, X.; Guo, Q.; Yang, J. Recyclable Polydopamine-Functionalized Sponge for High-Efficiency Clean Water Generation with Dual-Purpose Solar Evaporation and Contaminant Adsorption. *ACS Appl. Mater. Interfaces* **2019**, *11*, 32559−32568.
(33) Moloudi, M.; Rahmanifar, M. S.; Noori, A.; Chang, X.; Kaner, R. B.; Mousavi, M. F. Bioinspired Polydopamine Supported on Oxygen-Functionalized Carbon Cloth as a High-Performance 1.2 V Aqueous Symmetric Metal-Free Supercapacitor. *J. Mater. Chem. A* **2021**, *9*, 7712−7725.
(34) Kasbe, P. S.; Gade, H.; Liu, S.; Chase, G. G.; Xu, W. Ultrathin Polydopamine-Graphene Oxide Hybrid Coatings on Polymer Filters with Improved Filtration Performance and Functionalities. *ACS Appl. Bio Mater.* **2021**, *4*, 5180−5188.
(35) Meredith, P.; Sarna, T. The Physical and Chemical Properties of Eumelanin. *Pigm. Cell Res.* **2006**, *19*, 572−594.
(36) Ball, V. Impedance Spectroscopy and Zeta Potential Titration of Dopa-Melanin Films Produced by Oxidation of Dopamine. *Colloids Surf., A* **2010**, *363*, 92−97.
(37) Yang, N.; Yang, T.; Wang, W.; Chen, H.; Li, W. Polydopamine Modified Polyaniline-Graphene Oxide Composite for Enhancement of Corrosion Resistance. *J. Hazard. Mater.* **2019**, *377*, 142−151.
(38) Wang, X.; Lee, P. S. A Polydopamine Coated Polyaniline Single Wall Carbon Nanotube Composite Material as a Stable Supercapacitor Cathode in an Organic Electrolyte. *J. Mater. Res.* **2015**, *30*, 3575−3583.
(39) Zhu, M.; Jia, X.; Li, Y.; Zhao, C.; Chao, D.; Wang, C. A Cytocompatible Conductive Polydopamine towards Electrochromic Energy Storage Device. *Electrochim. Acta* **2021**, *374*, 137961.
(40) Huang, C.; Zhao, X.; Xu, Y.; Zhang, Y.; Yang, Y.; Hu, A.; Tang, Q.; Song, X.; Jiang, C.; Chen, X. Sewable and Cuttable Flexible Zinc-Ion Hybrid Supercapacitor Using a Polydopamine/Carbon Cloth-Based Cathode. *ACS Sustainable Chem. Eng.* **2020**, *8*, 16028−16036.
(41) Zhang, Z. J.; Deng, G. L.; Huang, X.; Wang, X.; Xue, J. M.; Chen, X. Y. Highly Boosting the Supercapacitor Performance by Polydopamine-Induced Surface Modification of Carbon Materials and Use of Hydroquinone as an Electrolyte Additive. *Electrochim. Acta* **2020**, *339*, 135940.
(42) Xu, W.; Qin, Z.; Chen, C. T.; Kwag, H. R.; Ma, Q.; Sarkar, A.; Buehler, M. J.; Gracias, D. H. Ultrathin Thermoresponsive Self-Folding 3D Graphene. *Sci. Adv.* **2017**, *3*, No. e1701084.
(43) Zeng, R.; Deng, H.; Xiao, Y.; Huang, J.; Yuan, K.; Chen, Y. Cross-Linked Graphene/Carbon Nanotube Networks with Polydopamine "Glue" for Flexible Supercapacitors. *Compos. Commun.* **2018**, *10*, 73−80.

https://doi.org/10.1021/acsaem.1c01996
ACS Appl. Energy Mater. 2021, 4, 10069−10080

(44) He, Y.; Dai, L.; Zhang, X.; Sun, Y.; Shi, W.; Ge, D. The Bioactive Polypyrrole/Polydopamine Nanowire Coating with Enhanced Osteogenic Differentiation Ability with Electrical Stimulation. *Coatings* **2020**, *10*, 1189.
(45) Kim, S.; Jang, L. K.; Jang, M.; Lee, S.; Hardy, J. G.; Lee, J. Y. Electrically Conductive Polydopamine-Polypyrrole as High Performance Biomaterials for Cell Stimulation in Vitro and Electrical Signal Recording in Vivo. *ACS Appl. Mater. Interfaces* **2018**, *10*, 33032−33042.
(46) Mihai, I.; Addiégo, F.; Del Frari, D.; Bour, J. Ô.; Ball, V. Associating Oriented Polyaniline and Eumelanin in a Reactive Layer-by-Layer Manner: Composites with High Electrical Conductivity. *Colloids Surf., A* **2013**, *434*, 118−125.
(47) Gospodinova, N.; Ivanov, D. A.; Anokhin, D. V.; Mihai, I.; Vidal, L.; Brun, S.; Romanova, J.; Tadjer, A. Unprecedented Route to Ordered Polyaniline: Direct Synthesis of Highly Crystalline Fibrillar Films with Strong π-π Stacking Alignment. *Macromol. Rapid Commun.* **2009**, *30*, 29−33.
(48) Chaudhari, H. K.; Kelkar, D. S. X-Ray Diffraction Study of Doped Polyaniline. *J. Appl. Polym. Sci.* **1996**, *62*, 15−18.
(49) Pouget, J. P.; Józefowicz, M. E.; Epstein, A. J.; Tang, X.; MacDiarmid, A. G. X-Ray Structure of Polyaniline. *Macromolecules* **1991**, *24*, 779−789.
(50) Lu, X.; Hlaing, H.; Germack, D. S.; Peet, J.; Jo, W. H.; Andrienko, D.; Kremer, K.; Ocko, B. M. Bilayer Order in a Polycarbazole-Conjugated Polymer. *Nat. Commun.* **2012**, *3*, 795.
(51) Su, Y. W.; Lin, Y. C.; Wei, K. H. Evolving Molecular Architectures of Donor-Acceptor Conjugated Polymers for Photovoltaic Applications: From One-Dimensional to Branched to Two-Dimensional Structures. *J. Mater. Chem. A* **2017**, *5*, 24051−24075.
(52) Wang, Y.; Sun, L.; Xiao, D.; Du, H.; Yang, Z.; Wang, X.; Tu, L.; Zhao, C.; Hu, F.; Lu, B. Silicon-Based 3D All-Solid-State Micro-Supercapacitor with Superior Performance. *ACS Appl. Mater. Interfaces* **2020**, *12*, 43864−43875.
(53) Liu, Y.; Ai, K.; Lu, L. Polydopamine and Its Derivative Materials: Synthesis and Promising Applications in Energy, Environmental, and Biomedical Fields. *Chem. Rev.* **2014**, *114*, 5057−5115.
(54) Yuan, Y.; Jiang, L.; Li, X.; Zuo, P.; Xu, C.; Tian, M.; Zhang, X.; Wang, S.; Lu, B.; Shao, C.; Zhao, B.; Zhang, J.; Qu, L.; Cui, T. Laser Photonic-Reduction Stamping for Graphene-Based Micro-Supercapacitors Ultrafast Fabrication. *Nat. Commun.* **2020**, *11*, 6185.
(55) Li, X.; Shen, J.; Sun, W.; Hong, X.; Wang, R.; Zhao, X.; Yan, X. A Super-High Energy Density Asymmetric Supercapacitor Based on 3D Core-Shell Structured NiCo-Layered Double Hydroxide@carbon Nanotube and Activated Polyaniline-Derived Carbon Electrodes with Commercial Level Mass Loading. *J. Mater. Chem. A* **2015**, *3*, 13244−13253.
(56) Liu, X.; Wen, N.; Wang, X.; Zheng, Y. A High-Performance Hierarchical Graphene@polyaniline@graphene Sandwich Containing Hollow Structures for Supercapacitor Electrodes. *ACS Sustainable Chem. Eng.* **2015**, *3*, 475−482.

https://doi.org/10.1021/acsaem.1c01996
ACS Appl. Energy Mater. 2021, 4, 10069−10080